中国科学: 技术科学
SCIENTIA SINICA Technologica
techcn.scichina.com
《中国科学》杂志社
SCIENCE CHINA PRESS
精选文章导读

高产率分级多孔Fe-N-C材料富集有效活性位点促进氧还原反应电催化动力学

杜泽轩[1†], 张梦帆[1,2†], 张文娟[3], 宋秉烨[1*], 苟倩誌[1*], 高然[1], 李安桂[1], 孙宪达[4]

1. 教育部低碳建筑环境国际合作联合实验室, 西安建筑科技大学建筑设备科学与工程学院, 西安 710055
2. 温州设计集团有限公司, 温州 325000
3. 西安稀有金属材料研究院有限公司, 西安 710016
4. 山东大学科学技术研究院, 济南 250061
† 同等贡献
* E-mail: bysong@xauat.edu.cn; gqz813@xauat.edu.cn

1 研究背景

氧还原反应(ORR)是燃料电池阴极的关键步骤, 其缓慢的动力学严重制约电池效率[1]. 目前, 商用铂基催化剂成本高、资源稀缺, 这限制了燃料电池的大规模应用[2]. 因此, 开发高性能、低成本的催化剂至关重要. 在众多非贵金属催化剂中, 铁-氮-碳(Fe-N-C)材料因其高活性和稳定性被视为最具潜力的铂替代品之一[3]. 其中, 以沸石咪唑骨架-8材料(ZIF-8)为前驱体的Fe-N-C催化剂备受关注[4]. 然而, 传统ZIF-8合成效率低, 而合成效率更高的ZIF-L则存在热稳定性差、热解后活性位点不均等问题, 导致催化性能不理想. 因此, 如何在高产率下制备具有丰富、稳定活性位点的Fe-N-C催化剂, 仍是当前面临的关键挑战.

2 本文工作

本文提出了一种拓扑自优化合成策略, 以在水相体系制备的叶状ZIF-L为前驱体, 含$Fe-N_4$结构的天然金属卟啉血红素为Fe源与活性位点供给体(图1(a)), 通过“共沉淀-拓扑结构优化-高温热解”三步法构建层级多孔Fe-N-C催化剂, 具体工作如下.

首先, 将硝酸锌与2-甲基咪唑溶于水形成溶液A, 血红素溶于DMF形成溶液B, A与B混合后室温共沉淀4 h后经离心得到Fe-ZIF-L前驱体; 随后在乙醇气氛下真空干燥24 h, 利用血红素中Fe与ZIF-L咪唑环中N的配位作用, 驱动Fe-ZIF-L自发转变为稳定的十二面体Fe-ZIF-8. 最后, 在N_2氛围下对Fe-ZIF-8进行高温热解, 得到Fe-N-C催化剂. 还探究了前驱体中血红素掺杂量(0、50、100、150 mg, 记为“x”)与热解温度(750、850、950、1050 °C, 记为“y”)对催化剂结构与ORR性能的影响, 催化剂命名为“Fe_x-N-C_y”.

通过扫描电子显微镜(SEM)、透射电子显微镜(TEM) (图1(b))、X射线光电子能谱(XPS, 图2(a)~(d))、氮气吸附-脱附(图2(e)和(f))等手段分析了催化剂的微观形貌、化学结构与孔隙特征. 采用旋转环盘电极(RRDE)在0.1 mol L^{-1} KOH溶液中测试了ORR催化活性(起始电位、半波电位、极限电流密度), 并评估催化剂稳定性与甲醇耐受性. 同时, 组装碱性直接乙醇燃料电池(DEFC), 验证催化剂的实际应用性能.

3 本文结论

通过拓扑自优化策略, Fe-N-C催化剂产量显著提

英文全文见: Du Z X, Zhang M F, Zhang W J, et al. High yielding hierarchical porous Fe-N-C with enriched effective active sites: Promoting oxygen reduction reaction electrocatalytic kinetics. Sci China Technol Sci, 2025, 68: 1520208, https://doi.org/10.1007/s11431-024-2890-3

© 2026《中国科学》杂志社

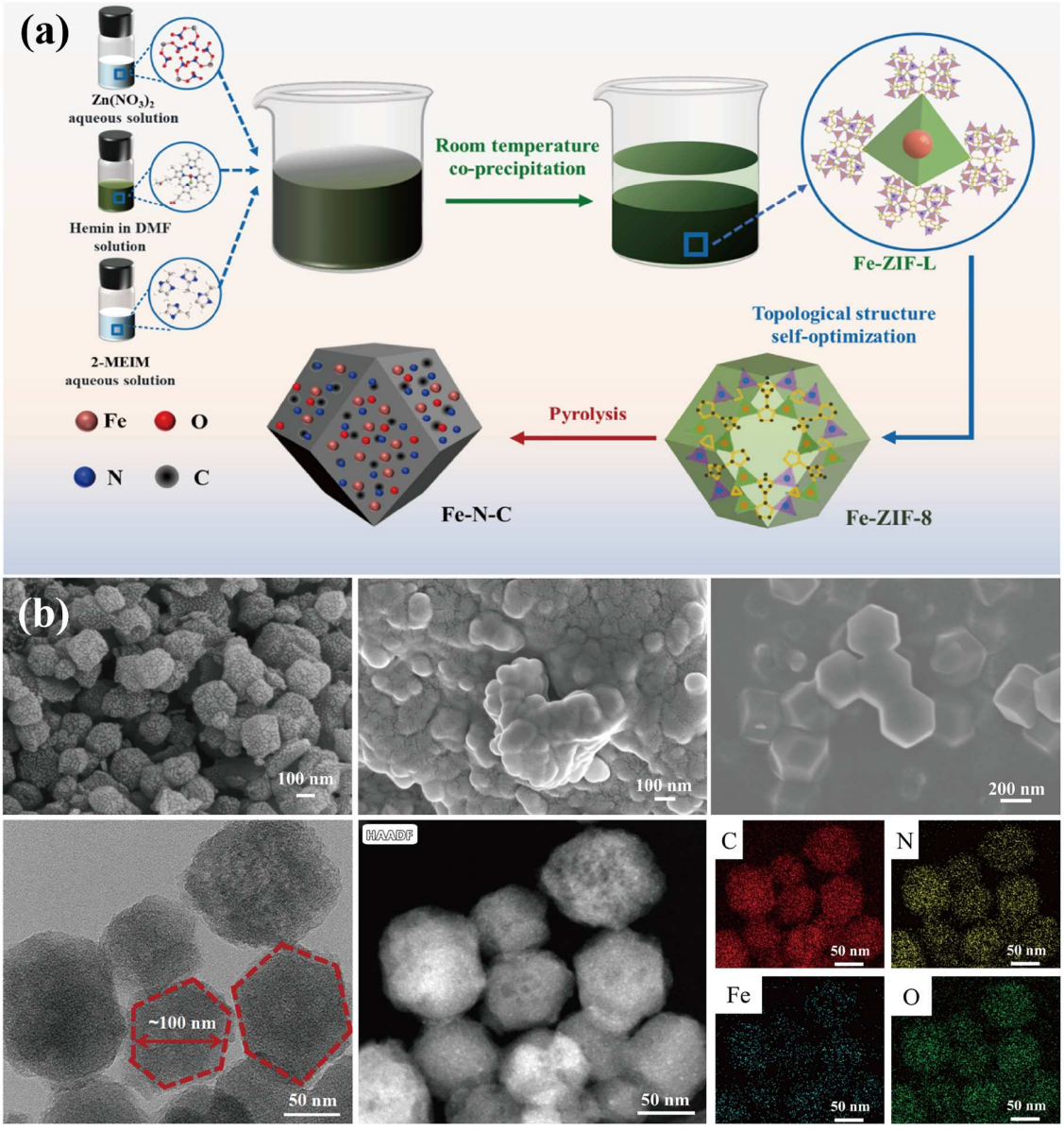


图 1 (网络版彩图) (a) Fe-N-C催化剂制备流程示意图; (b) 催化剂微观结构表征
Figure 1 (Color online) (a) Synthesis process of Fe-N-C catalyst; (b) microstructural characterization of catalysts.

升, 以最优工艺合成的Fe_{100}-N-C_{950}, 产量是传统甲醇体系下合成产物的3.72倍. 结构表征显示, Fe_{100}-N-C_{950}呈现均匀的十二面体形貌, 表面具有沟槽状特征, 比表面积达663.81 $m^2\ g^{-1}$, 介孔体积为0.81 $cm^3\ g^{-1}$, 形成微-介孔共存的梯级孔隙结构, 可有效暴露活性位点并降低传质阻力[5]. XPS证实其含丰富且均匀的吡啶N与Fe-N_x活性位点.

Fe_{100}-N-C_{950}的ORR催化性能全面优于商业Pt-C催化剂. 如图3(a)和(b)所示, 在碱性介质中, 其起始电位为1.054 V (vs. RHE)、半波电位为0.847 V (vs. RHE), 分别高于商业Pt-C的0.952与0.820 V; 极限电流密度达−5.77 mA cm^{-2}, 优于Pt-C的−4.967 mA cm^{-2}; 塔菲尔斜率为63.92 mV dec^{-1}, 低于Pt-C的75.39 mV dec^{-1}, 催化动力学更优(图3(c)). 且具有最小的电化学阻抗(electrochemical impedance spectroscopy, EIS)阻抗圆弧(图3(d)).

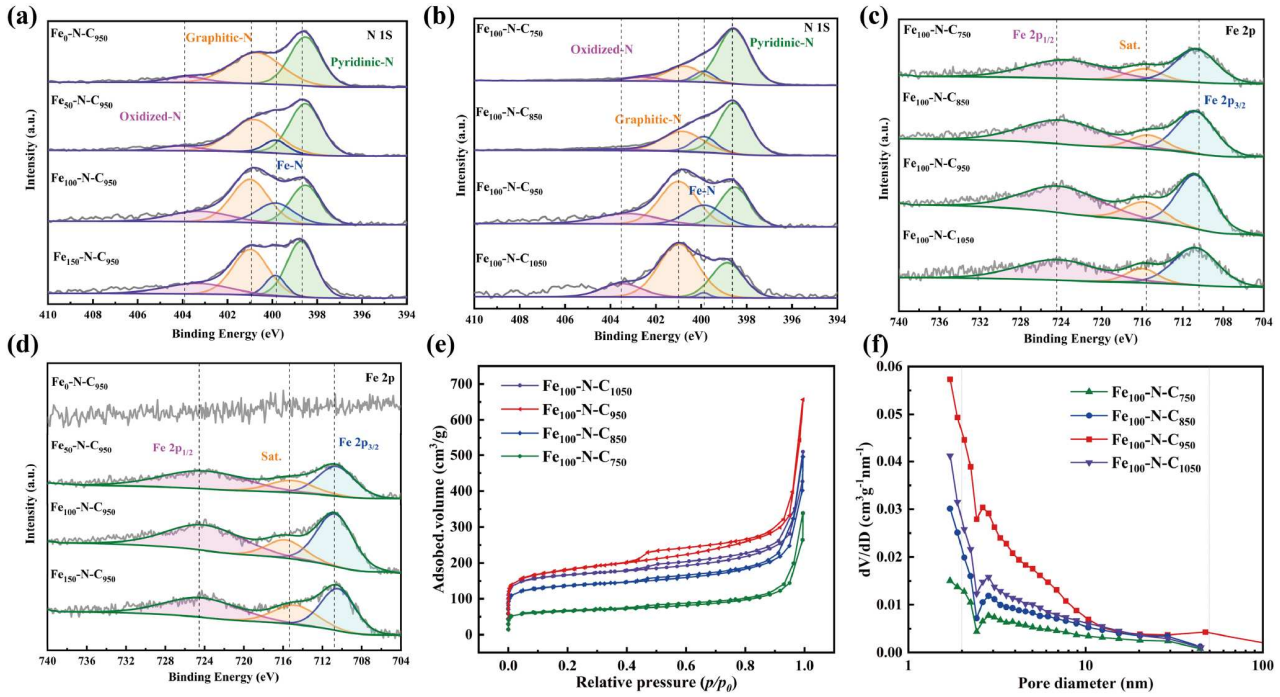


图 2 (网络版彩图) (a) 不同血红素掺杂水平制备的Fe_x-N-C_{950}的XPS高分辨率N 1s谱图; (b) 不同热解温度下制备的Fe_{100}-N-C_y的N 1s谱; (c) Fe_x-N-C_{950}的Fe 2p光谱; (d) Fe_{100}-N-C_y的Fe 2p光谱; (e) 不同热解温度下制备的Fe_{100}-N-C_y的N_2吸附曲线; (f) 通过Barrett-Joyner-Halenda (BJH)方法测定不同热解温度下制备的Fe_{100}-N-C_y的孔径尺寸分布

Figure 2 (Color online) (a) N 1s spectrum of Fe_x-N-C_{950} prepared with different hemin doped levels; (b) N 1s spectrum of Fe_{100}-N-C_y prepared at different pyrolysis temperatures; (c) Fe 2p spectrum of Fe_x-N-C_{950}; (d) Fe 2p spectrum of Fe_{100}-N-C_y; (e) N_2 adsorption curves of Fe_{100}-N-C_y prepared at different pyrolysis temperatures; (f) mesopore size distribution determined by the BJH method of Fe_{100}-N-C_y prepared at different pyrolysis temperatures.

稳定性测试显示, 40000 s后Fe_{100}-N-C_{950}仍保留89.4%的初始电流密度, 而Pt-C仅保留75.1% (图3(e)), 且Fe_{100}-N-C_{950}对甲醇无响应, 具备良好的甲醇耐受性(图3(f)), 可避免燃料电池甲醇渗透问题.

为了研究Fe_{100}-N-C_{950}催化剂的ORR机制, 使用RRDE研究了ORR过程, 如图3(g)所示. 结果表明, Fe_{100}-N-C_{950}催化剂ORR过程的电子转移数在3.76~3.976之间, 且H_2O_2产率低, 表明典型的四电子转移动力学机制.

将Fe_{100}-N-C_{950}用作DEFC阴极催化剂, 电池开路电压达0.88 V, 高于Pt-C的0.74 V, 峰值功率密度22.37 mW cm^{-2}, 展现出良好的实际应用潜力(图3(h)). 通过比较Fe_{100}-N-C_{950}与其他报道的电催化剂在碱性溶液中的ORR催化性能[6~19], 如图3(i)所示, Fe_{100}-N-C_{950}催化剂表现出优异的ORR催化活性.

本文采用拓扑优化方法以ZIF-L为前驱体合成了具有优异ORR催化活性的十二面体多孔Fe-N-C催化剂. 所得催化剂的产率比甲醇环境下合成的Fe-N-C材料高3.72倍. 研究了血红素掺杂量和热解温度对Fe-N-C催化性能的影响. 实验结果表明, 热解温度950 °C、血红素掺杂量100 mg合成的Fe_{100}-N-C_{950}催化剂具有丰富且均匀分布的吡啶-N和Fe-N_x活性位点. 催化剂具有663.81 m^2 g^{-1}的大比表面积, 使得活性位点得以充分暴露, 从而增加了电化学活性表面积. 由于丰富的介孔和微孔结构以及高石墨碳含量, 氧气、离子和电子的传质阻力得以降低. 在相同负载量下, 与商用Pt-C催化剂相比, Fe_{100}-N-C_{950}表现出显著增强的ORR催化效率和稳定性. 此外, 以Fe_{100}-N-C_{950}作为阴极催化剂的碱性DEFC表现出比商业Pt-C略高的峰值功率密度.

综上, 本研究通过拓扑自优化策略, 成功解决了Fe-N-C催化剂产量低、活性位点分散性差的瓶颈, 为燃料电池非贵金属催化剂的商业化应用提供了可行方案.

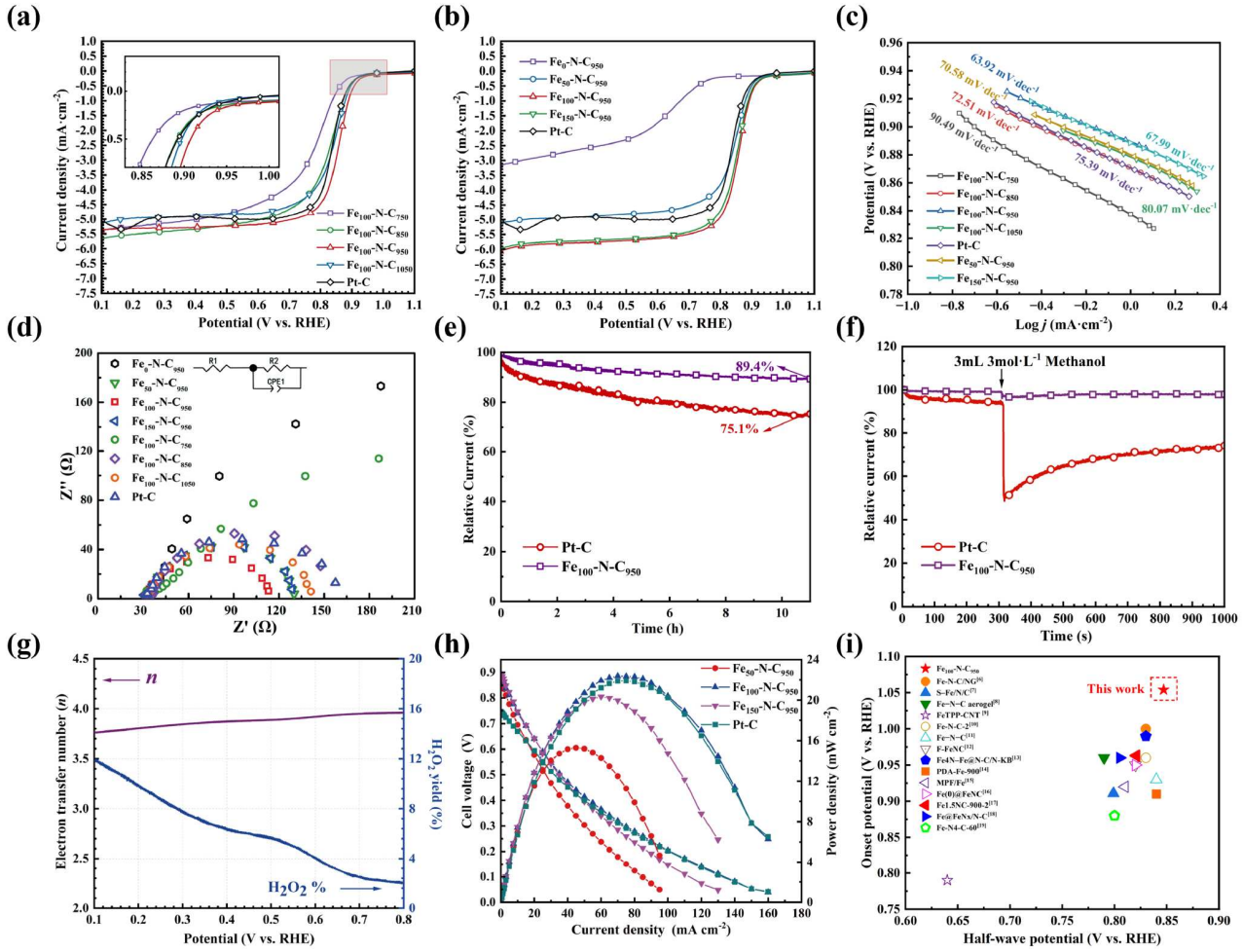


图 3 (网络版彩图) (a) Fe$_{100}$-N-C$_y$ 线性扫描伏安(LSV)在曲线O_2饱和的0.1 mol L^{-1} KOH中, 1600 r min^{-1}下的测试曲线; (b) Fe$_x$-N-C$_{950}$ LSV测试曲线; (c) 所有制备的Fe-N-C催化剂的塔菲尔曲线; (d) 所有制备的Fe-N-C在0.87 V (vs. RHE)电位下的EIS测试曲线; (e) Fe$_{100}$-N-C$_{950}$催化剂在0.80 V下40000 s的耐久性测试; (f) Fe$_{100}$-N-C$_{950}$催化剂的耐甲醇性测试; (g) Fe$_{100}$-N-C$_{950}$和Pt-C的电子转移数n和H_2O_2生成速率; (h) AEM-DEFC功率密度和电流-电压曲线(阳极: 1 mL min^{-1}, 3 mol L^{-1} KOH和3 mol L^{-1} CH_3CH_2OH; 阴极: 10 sccm氧气; 60 °C); (i) Fe$_{100}$-N-C$_{950}$与其他报道的电催化剂在碱性溶液中的催化性能比较[6~19]

Figure 3 (Color online) (a) Fe$_{100}$-N-C$_y$ linear sweep voltammetry (LSV) test curves in O_2-saturated 0.1 mol L^{-1} KOH at 1600 r min^{-1}; (b) Fe$_x$-N-C$_{950}$ LSV test curves; (c) Tafel curves for all the prepared Fe-N-C catalysts; (d) EIS test curves of all the prepared Fe-N-C with the potential at 0.87 V (vs. RHE); (e) durability test for Fe$_{100}$-N-C$_{950}$ catalysts at 0.80 V for 40000 s; (f) methanol resistance test for Fe$_{100}$-N-C$_{950}$ catalysts; (g) the electron transfer number n and H_2O_2 production rate of Fe$_{100}$-N-C$_{950}$ and Pt-C; (h) AEM-DEFC power density and current-voltage curves (anode: 1 mL min^{-1} of 3 mol L^{-1} KOH and 3 mol L^{-1} CH_3CH_2OH; cathode: 10 sccm of oxygen; 60 °C); (i) comparison of the catalytic performance of Fe$_{100}$-N-C$_{950}$ with other electrocatalysts reported in alkaline solutions [6–19].

参考文献

1 Xue D P, Yuan Y F, Yu Y, et al. Spin occupancy regulation of the Pt d-orbital for a robust low-Pt catalyst towards oxygen reduction. Nat Commun, 2024, 15: 5990

2 Luo H R, Gou Q Z, Zheng Y J, et al. Machine learning-assisted high-donor-number electrolyte additive screening toward construction of dendrite-free aqueous zinc-ion batteries. ACS Nano, 2025, 19: 2427–2443

3 Xue J L, Li Y S, Hu J. Nanoporous bimetallic Zn/Fe–N–C for efficient oxygen reduction in acidic and alkaline media. J Mater Chem A, 2020, 8: 7145–7157

4 Song B Y, Li M J, Yang Y W, et al. Achievement of a novel porous non-noble-metal catalyst with excellent oxygen reduction reaction activity: Promoting the commercialization of alkaline fuel cells. J Clean Prod, 2020, 249: 119314

5 Deng J B, Luo H R, Gou Q Z, et al. Subnanocyclic molecule of 15-crown-5 inhibiting interfacial water decomposition and stabilizing zinc anodes via regulation of Zn^{2+} solvation shell. J Phys Chem Lett, 2023, 14: 9167–9175

6 Wang T, Feng J, Liu Q, et al. Facile synthesis of amino acids-derived Fe/N-codoped reduced graphene oxide for enhanced ORR electrocatalyst. J Electroanal Chem, 2022, 915: 116326

7 Hu K, Tao L, Liu D, et al. Sulfur-doped Fe/N/C nanosheets as highly efficient electrocatalysts for oxygen reduction reaction. ACS Appl Mater Interfaces, 2016, 8: 19379–19385

8 Wang Y, Tu R, Hou C, et al. Porous Fe-N-C aerogels derived from metal-organic aerogels as electrocatalysts for the oxygen reduction reaction. ChemPlusChem, 2022, 87: e202200312

9 Li Q, Xu Y, Pedersen A, et al. Investigating the role of Fe-pyrrolic N4 configuration in the oxygen reduction reaction via covalently bound porphyrin functionalized carbon nanotubes. Adv Funct Mater, 2024, 34: 2311086

10 Li J, Lin M, Huang W, et al. Pomegranate-like Fe-N-C with optimized Fe-N_4 configuration as Bi-functional catalysts for rechargeable zinc-air batteries. Small Meth, 2023, 7: 2201664

11 Ricciardi B, Mecheri B, da Silva Freitas W, et al. Porous iron-nitrogen-carbon electrocatalysts for anion exchange membrane fuel cells (AEMFC). ChemElectroChem, 2023, 10: e202201115

12 Yang T, Chen Y, Tian M, et al. Engineering the electronic structure of Fe-N/C catalyst via fluorine self-doping for enhanced oxygen reduction reaction in liquid and all-solid-state Zn-air batteries. Electrochim Acta, 2023, 443: 141907

13 Zhang X, Su K, Chen X, et al. A hybrid of the Fe_4N–Fe heterojunction supported on N-doped carbon nanobelts and Ketjen Black carbon as a robust high-performance electrocatalyst. J Phys Chem Lett, 2022, 13: 11118–11127

14 Zhang F, Liu X, Chen Y, et al. Ordered mesoporous carbon fiber bundles with high-density and accessible Fe-N_x active sites as efficient ORR catalysts for Zn-air batteries. Chin Chem Lett, 2023, 34: 108142

15 Akula S, Mooste M, Kozlova J, et al. Transition metal (Fe, Co, Mn, Cu) containing nitrogen-doped porous carbon as efficient oxygen reduction electrocatalysts for anion exchange membrane fuel cells. Chem Eng J, 2023, 458: 141468

16 Li Z, Wei L, Jiang W J, et al. Chemical state of surrounding iron species affects the activity of Fe-N_x for electrocatalytic oxygen reduction. Appl Catal B-Environ, 2019, 251: 240–246

17 Li X, Zhao Y, Yang Y, et al. A universal strategy for carbon-based ORR-active electrocatalyst: One porogen, two pore-creating mechanisms, three pore types. Nano Energy, 2019, 62: 628–637

18 Chen Y, Shi Z, Wang Z, et al. Yolk-shell Fe@FeN_x nanoparticles decorated N-doped mesoporous carbon as highly active electrocatalyst for oxygen reduction reactions. J Alloys Compd, 2020, 829: 154558

19 Wang X, Jia Y, Mao X, et al. Edge-rich Fe-N_4 active sites in defective carbon for oxygen reduction catalysis. Adv Mater, 2020, 32: 2000966